OPEN

NPG Asia Materials (2016) 8, e302; doi:10.1038/am.2016.134
www.nature.com/am

ORIGINAL ARTICLE

Attaining high mid-temperature performance in $(Bi,Sb)_2Te_3$ thermoelectric materials via synergistic optimization

Zhaojun Xu[1], Haijun Wu[2,3], Tiejun Zhu[1], Chenguang Fu[1], Xiaohua Liu[1], Lipeng Hu[1], Jian He[4], Jiaqing He[2] and Xinbing Zhao[1]

For decades, zone-melted Bi_2Te_3-based alloys have been the most widely used thermoelectric materials with an optimal operation regime near room temperature. However, the abundant waste heat in the mid-temperature range poses a challenge; namely, *how* and *to what extent* the service temperature of Bi_2Te_3-based alloys can be upshifted to the mid-temperature regime. We report herein a synergistic optimization procedure for Indium doping and hot deformation that combines intrinsic point defect engineering, band structure engineering and multiscale microstructuring. Indium doping modulated the intrinsic point defects, broadened the band gap and thus suppressed the detrimental bipolar effect in the mid-temperature regime; in addition, hot deformation treatment rendered a multiscale microstructure favorable for phonon scattering and the donor-like effect helped optimize the carrier concentration. As a result, a peak value of zT of ~ 1.4 was attained at 500 K, with a state-of-the-art average zT_{av} of ~ 1.3 between 400 and 600 K in $Bi_{0.3}Sb_{1.625}In_{0.075}Te_3$. These results demonstrate the efficacy of the multiple synergies that can also be applied to optimize other thermoelectric materials.

NPG Asia Materials (2016) **8,** e302; doi:10.1038/am.2016.134; published online 2 September 2016

INTRODUCTION

Thermoelectricity is the simplest technology for direct heat-to-electricity power generation. Thermoelectric (TE) devices are all solid state, without rotation parts or working fluids, and are thus easy to miniaturize. These modular characteristics make TE devices reliable, durable and easy to use in tandem with other energy conversion technologies.[1,2] The energy conversion efficiency of a TE device is primarily determined by the TE material's dimensionless figure of merit, defined as $zT = \alpha^2\sigma T/\kappa$, where α is the Seebeck coefficient, σ is the electrical conductivity, κ is the total thermal conductivity (including the lattice contribution κ_L and the carrier contribution κ_e) and T is the absolute temperature.[2] zT is generally a function of temperature whereas waste heat is the energy source for TE power generation. It is useful to compare the optimal operation temperature ('service temperature') of state-of-the-art TE materials and the temperature range in which most of the waste heat is produced. State-of-the-art TE materials have their best zT values (those between 1 and 2) in different temperature regimes; for example, Bi_2Te_3 works best near room temperature,[3,4] whereas PbTe, $Mg_2Si_{1-x}Sn_x$, Half-Heusler compounds and filled skutterudites generally reach their best performance above 600 K.[5–14] There is a conspicuous lack of high-performance TE materials between 400 and 600 K, the mid-temperature range. Meanwhile, most of the waste heat produced (including various industrial sectors and automobile exhausts) is in the temperature range of 400–900 K, and hence it is unharvested.[15–17] Therefore, developing high-performance mid-temperature TE materials in the temperature range 400–600 K is of significant value in practice.[1,2,18–20] The goal of this work is to shift the service temperature of Bi_2Te_3-based alloys from near room temperature to the mid-temperature range while maintaining a high average zT value.

Bi_2Te_3-based alloys have been the benchmark commercial TE material for decades. Zone-melted (ZM) Bi_2Te_3-based alloys exhibit $zT \sim 1$ near room temperature, making them the only TE material used for both power generation and refrigeration. The materials have also been thoroughly studied in terms of their associated sources of parasitic losses, the trade-off between TE performance and mechanical properties and electrode fabrication.[4] It is therefore ideal to upshift the service temperature of Bi_2Te_3-based alloys from near room temperature to the mid-temperature range. There have been some previous efforts to this end. Wang *et al.*[21] reported a peak zT value of ~ 0.86 at 600 K in *n*-type $Bi_2Te_{1.5}Se_{1.5}$, Liu *et al.*[22] obtained a peak zT value of ~ 0.8 at 573 K in *n*-type Bi_2Te_2S and a peak zT value of ~ 0.92 at 710 K was attained in *p*-type $Ag_{0.01}Sb_{1.85}In_{0.15}Te_3$ alloy by Hua *et al.*[23]

[1]State Key Laboratory of Silicon Materials, School of Materials Science and Engineering, Zhejiang University, Hangzhou, China; [2]Department of Physics and Shenzhen Key Laboratory of Thermoelectric Materials, South University of Science and Technology of China, Shenzhen, China; [3]Department of Materials Science and Engineering, National University of Singapore, Singapore, Singapore and [4]Department of Physics and Astronomy, Clemson University, Clemson, SC, USA
Correspondence: Professor T Zhu, State Key Laboratory of Silicon Materials, School of Materials Science and Engineering, Zhejiang University, 38 Zheda Road, Hangzhou 310027, China.
E-mail: zhutj@zju.edu.cn
Received 14 April 2016; revised 29 June 2016; accepted 30 June 2016

However, none of these zT values exceeds 1, which is the customary criterion for practical applications, in the range of 400–600 K.

The performance degradation of Bi_2Te_3-based alloys at elevated temperatures arises from the intrinsically small band gap E_g of Bi_2Te_3 (~ 0.13 eV).[24,25] Given such a small band gap, the minority carriers are more easily thermally excited, and the resulting detrimental bipolar effect not only decreases the Seebeck coefficient but also introduces extra thermal conductivity that results in a decreased zT.[26] Therefore, to increase the service temperature of Bi_2Te_3-based alloys, one must first broaden the E_g. Because the E_g of Sb_2Te_3 is ~0.28 eV,[27,28] doping Sb in Bi_2Te_3 becomes a natural approach. Sb doping also helps optimize the carrier concentration and introduces strong point defect scattering of heat-carrying phonons, thus favoring a higher zT. However, there is an inherent restriction of Sb doping: doping with too high a content of Sb will lead to too great a hole concentration because of the reduced formation energy of antisite defects,[29,30] resulting in a reduced α and an increased κ_e. Indium (In) doping helps mitigate this limitation. We found that In doping could efficiently broaden the band gap of Sb_2Te_3 and upshift the service temperature to higher temperatures without significant side effects.[23] Building on these results, in this work, we intend to co-dope Bi_2Te_3 with Sb and In.

The defect chemistry of Sb and In doping in Bi_2Te_3 is intrinsically interesting.[31] Sb and In dopants (extrinsic point defects) modulate intrinsic point defects (mainly antisite defects) that in turn govern the electrical and thermal properties of the material. Intrinsic point defects are the primary determinant of the thermoelectric properties, and Sb and In dopants are the 'precursors'. Therefore, the goal of upshifting the service temperature in this work is translated into how to conduct intrinsic point defect engineering via extrinsic Sb and In doping.[13,32–34] Intrinsic point defects are primarily entropic defects. They are thermally more robust than extrinsic point defects and therefore favor robust high-temperature performance.

Doping, either single or multiple, finely tunes the key electrical parameters such as the valley degeneracy, carrier concentration, effective mass, deformation potential and band gap.[6,23,26,35,36] However, doping alone may not be sufficient to attain a zT higher than 1 in a material as mature as Bi_2Te_3. With respect to the lattice thermal conductivity, one must tailor the microstructure on multiple length scales to comprehensively scatter heat-carrying phonons with different wavelengths and frequencies.[5,37–39]

More importantly, intrinsic point defect engineering, band structure engineering and microstructuring must be implemented in a concerted, synergistic way. In this work, we chose the composition $Bi_{0.3}Sb_{1.7}Te_3$ that has a higher Sb content and, thus, a higher E_g compared with the widely used commercial $Bi_{0.5}Sb_{1.5}Te_3$. Indium was doped to (1) further widen the band gap and (2) optimize the concentration of the intrinsic point defect. In particular, hot

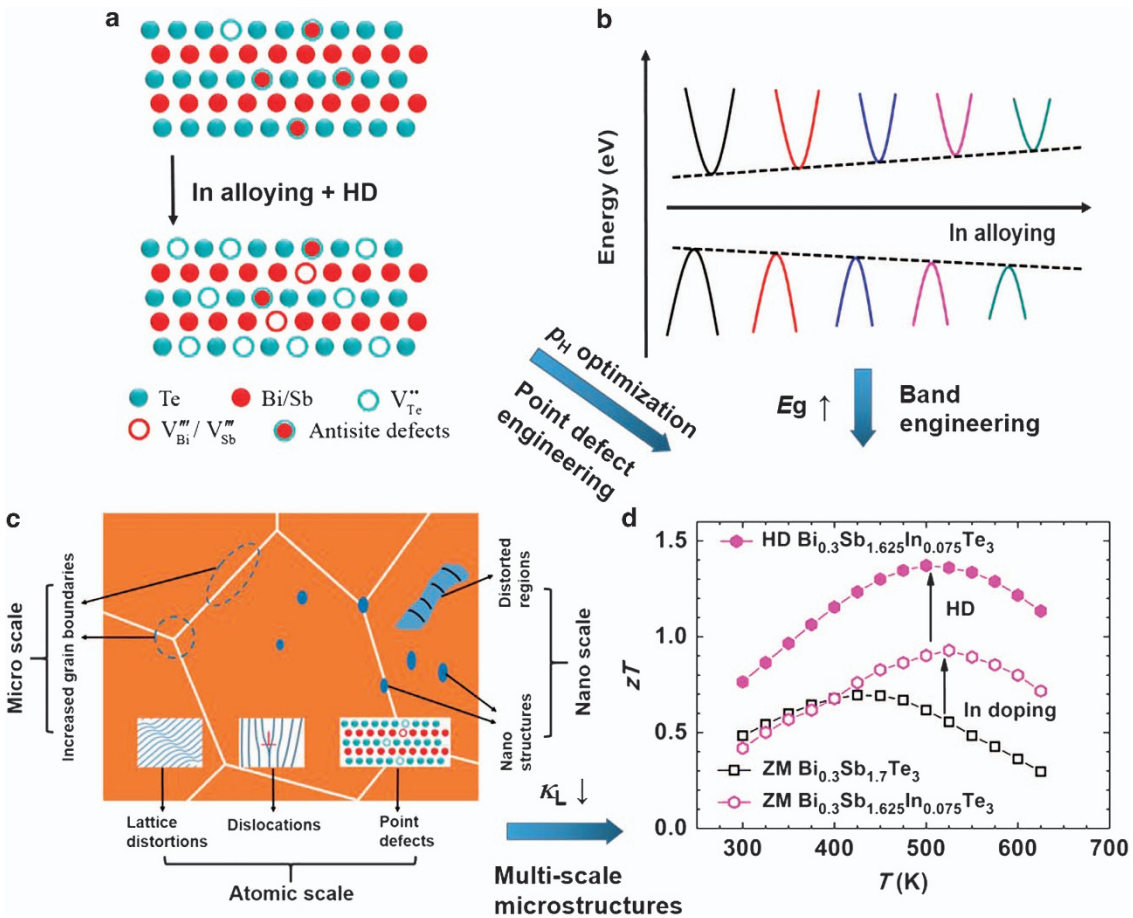

Figure 1 High zT for mid-temperature power generation via synergistically implementing point defects, hot deformation (HD) and Indium (In) doping. (**a**) A schematic illustration showing the increased number of vacancies and decreased number of antisite defects after In doping and HD. (**b**) A schematic showing the increased band gap after In doping. The shift of the band edge is for illustration purpose only. (**c**) A schematic illustration showing the multiscale microstructures after HD and (**d**) a comparison of the zT values of zone-melted (ZM) $Bi_{0.3}Sb_{1.7}Te_3$, ZM $Bi_{0.3}Sb_{1.625}In_{0.075}Te_3$ and HD $Bi_{0.3}Sb_{1.625}In_{0.075}Te_3$.

deformation (HD) processing was employed to further optimize the intrinsic point defect concentration via the donor-like effect and to create multiscale phonon scattering centers. As a result, a maximum zT of ~ 1.4 at 500 K and an average zT of ~ 1.3 between 400 and 600 K were obtained for hot deformed $Bi_{0.3}Sb_{1.625}In_{0.075}Te_3$.

EXPERIMENTAL PROCEDURES

High-purity elemental chunks of 99.999% Bi, 99.999% Sb, 99.999% Te and 99.999% In were used as starting materials. Appropriate quantities of elements were weighed according to the nominal composition of $Bi_{0.3}Sb_{1.7-x}In_xTe_3$ ($x = 0$, 0.025, 0.05, 0.075 and 0.1), mixed and sealed in an evacuated quartz tube at 10^{-3} Pa. The admixture was melted at 1023 K in a rocking furnace to ensure composition homogeneity and was then furnace-cooled to room temperature. The products were used in a zone melting furnace at a temperature gradient of 30 K cm^{-1} and a growth rate of 20 mm h^{-1}. Then, the ZM ingots were annealed at 473 K for 48 h. The resulting ingots consisted of coarse grains with the (00l) planes aligned approximately parallel to the growth direction. The initial ZM ingot with In content x was hereafter named ZM-In$_x$. The electrical and thermal properties were tested along the growth direction of the ingot unless otherwise noted.

HD processing was then performed. The ZM ingot with diameter of 16 mm was loaded in a graphite die of ϕ 20 mm, and a pressure of 80 MPa was applied at 823 K for 30 min. The deformation pressure was always applied along the longitudinal direction of the rod (same as the growth direction of ingot). Additional experimental details of HD processing can be found elsewhere.[3,23,38,40,41] Finally, disk-shaped hot deformed samples of 20 mm were acquired and named HD-In$_x$. All of the samples have similar densities of ~ 95% of the theoretical values. As demonstrated in our previous work, the thermoelectric properties of the HD samples are practically isotropic.[41] In this work, the results of the HD samples measured perpendicular to the pressure direction are presented.

The phase structure of all samples was investigated by X-ray diffraction on a Rigaku D/MAX-2550P diffractometer (Hangzhou, China). The X-ray diffraction patterns show that all of the ZM $Bi_{0.3}Sb_{1.7-x}In_xTe_3$ samples with $x = 0$, 0.025, 0.05, 0.075 and 0.10 were pure and lacked any detectable secondary phases (Supplementary Figure S1). The freshly fractured surfaces were observed using a FEI Sirion field emission scanning electron microscope. Transmission electron microscopy (TEM) investigations were performed on a FEI Tecnai G^2 200 kV TEM microscope (Hangzhou, China). The thin TEM specimens were prepared using the conventional standard methods and focused ion beam under low current in FEI Helios NanoLab 600i. The conventional procedures include cutting, grinding, dimpling, polishing and Ar-ion milling on a liquid nitrogen cooling stage.

The Seebeck coefficient α and electrical conductivity σ were measured simultaneously on a commercial Linseis LSR-3 system (Hangzhou, China). The thermal diffusivity D and the specific heat capacity C_P were measured on a Netzsch LFA 457 laser flash apparatus (Hangzhou, China) with a Pyroceram standard. The density ρ_D was estimated by an ordinary dimension and weight measurement procedure. The thermal conductivity was then calculated using the relation $\kappa = D\rho_D C_P$. The Hall coefficient R_H was measured at 300 K on a Quantum Design PPMS-9T using a four-probe configuration,

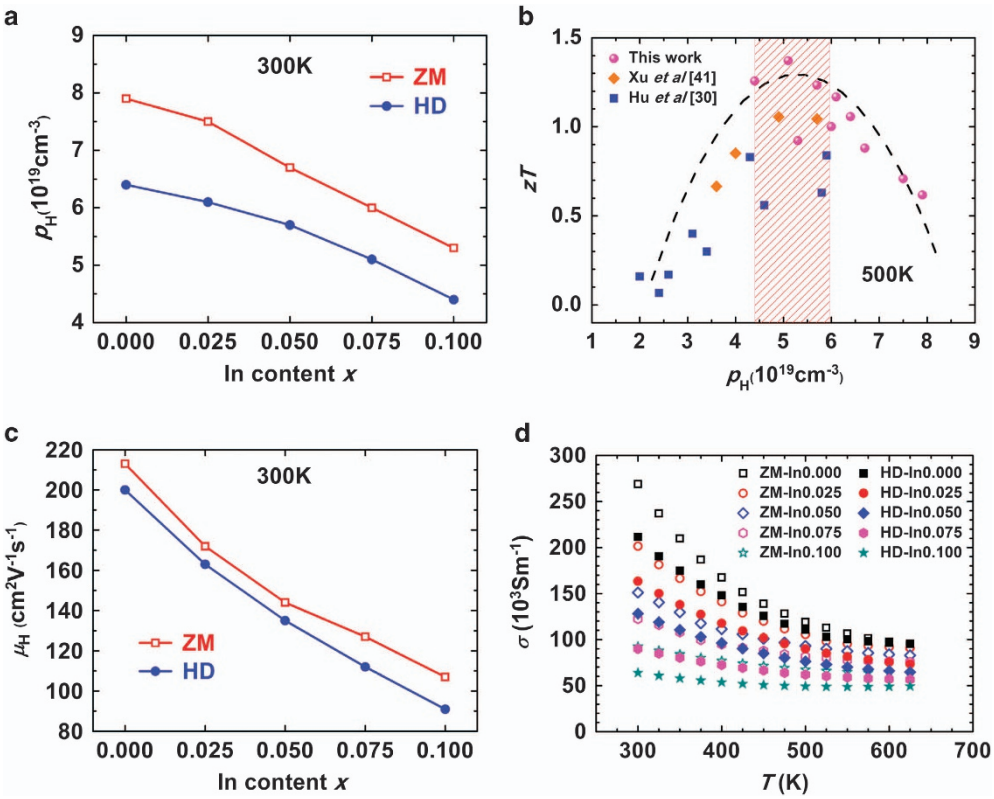

Figure 2 (**a**) Hole concentration p_H as a function of Indium (In) content x in $Bi_{0.3}Sb_{1.7-x}In_xTe_3$ samples before and after hot deformation (HD). (**b**) zT values at 500 K as a function of hole concentration p_H in p-type (Bi, Sb)$_2$Te$_3$ alloys in our prior work.[30,41] (**c**) Room temperature Hall mobility μ_H as a function of In content x in $Bi_{0.3}Sb_{1.7-x}In_xTe_3$ samples before and after HD. (**d**) Temperature dependence of electrical conductivity σ of zone-melted (ZM) and HD $Bi_{0.3}Sb_{1.7-x}In_xTe_3$ samples.

with the magnetic field sweeping between ±4.0 T. The carrier concentration n and the carrier mobility μ were estimated via the relationships $p_H = -1/(eR_H)$ and $\mu_H = R_H\sigma$, respectively.

To determine the band gap, samples were measured using a Harrick 'Praying Mantis' Research diffuse reflectance accessory (Hangzhou, China) on a VERTEX 70 Fourier transform infrared spectrometer (Hangzhou, China) with a MCT detector and a KBr beamsplitter. The absorption coefficient was obtained using Kubelka–Munk analysis,

$$F(R) = \frac{A}{K} = \frac{(1-R)^2}{2R} \quad (1)$$

where R is the fractional reflectance, A is the absorption coefficient and K is the scattering coefficient.[42]

RESULTS AND DISCUSSION

Synergistic approach to enhancing zT in mid-temperature range

As illustrated in Figure 1, intrinsic point defect engineering, electron band structure engineering and multiscale microstructures are synergistically implemented to achieve high mid-temperature performance p-type $(Bi,Sb)_2Te_3$. We first discuss the defect chemistry. The increased number of vacancies and decreased number of antisite defects after In doping and HD are illustrated in Figure 1a. When synthesizing p-type $(Bi,Sb)_2Te_3$ from stoichiometric raw materials, Bi and Sb atoms tend to occupy Te vacancies and form the negatively charged antisite defects Bi'_{Te} and Sb'_{Te}. These intrinsic point defects formed during the crystal growth are responsible for the p-type conductive characteristic.[29,43] The formation energy of the antisite defects depends on the bond polarity that is in turn related to the electronegativity χ difference between the constituent atoms.[29,43] In doping reduced the hole concentration p_H because of the greater difference in χ of In-Te than of Sb-Te (Supplementary Table S1). In addition, HD processing reduced the p_H because of the donor-like effect[3,41] that is also related to the intrinsic point defect engineering. As shown in Figure 1b, the band gap increases with In doping. A larger band gap thus suppresses the detrimental bipolar effect and upshifts the service temperature.

Notwithstanding the complex relationship between the κ_L and the microstructures, the reduction of κ_L could be attributed to three primary types of microstructures (Figure 1c). First, the increased microscale grain boundaries in the HD sample (as compared with the ZM sample) enhance the scattering of long-wavelength (low-frequency) phonons. Second, the nanostructures that are formed *in situ* via dynamic recrystallizations in HD processing[3,41] contribute to the scattering of phonons with middle wavelengths (middle frequencies). Third, HD-induced dislocations and other lattice distortions, along with intrinsic and extrinsic point defects, scatter the short-wavelength (high-frequency) phonons.[3,38,40] Defects V'''_{Bi}(or V'''_{Sb}) and $V^{\bullet\bullet}_{Te}$ are effective scatters of short-wavelength (high-frequency) phonons because of the larger mass and size differences between the occupied sites and the vacancies.[32,44] Therefore, these multiscale microstructures effectively reduce the κ_L over a wide temperature range. As a result, a maximum zT of ~ 1.4 at 500 K and an average zT_{av} ~ 1.3 between 400 and 600 K are achieved in $Bi_{0.3}Sb_{1.625}In_{0.075}Te_3$ upon In doping and HD in this work (Figure 1d), demonstrating the promise of these materials for mid-temperature power generation.

Carrier concentration and electrical properties

In Bi_2Te_3-based compounds, the carrier concentration is the most important physical quantity for TE performance. Figure 2a shows the In content dependence of carrier concentration p_H for all of the ZM and HD $Bi_{0.3}Sb_{1.7-x}In_xTe_3$ samples. The hole concentration p_H decreases as the In content increases, suggesting that substituting In ($5s^25p^1$) on Sb ($5s^25p^3$) sites does not produce more holes as expected. According to the literature,[45,46] only the 5p orbitals of Sb and Te contribute to the formation of σ-bonds in Sb_2Te_3 and the incorporation of In into Sb_2Te_3 lattice generates uncharged defects$In^{\times}_{Sb}$via the electronic transition:[45] $In(5s^25p^1) \rightarrow In^{\times}_{Sb}(5s^05p^3)$. Because of the greater difference in χ of In-Te than that of Sb-Te (Supplementary Table S1), In doping suppresses the formation of antisite defects, as was demonstrated in our early study of Sb_2Te_3.[23] Meanwhile, Te vacancies are increased because of the incorporation of In in the host.[31] As a result, the hole concentration is reduced.[23,31,45] This observation is also consistent with the results obtained in an early study of $(Sb_{0.75}Bi_{0.25})_{2-x}In_xTe_3$ single crystals (Supplementary Figure S2).[31]

The p_H of the HD samples is systematically lower than that of the ZM samples because of the donor-like effect.[47,48] The non-basal slip during the deformation processing (typically upon HD) tends to create 3Te–2Bi vacancy–interstitial pairs,[49] and the $\mathbf{Bi}'_{Te}$ will more readily diffuse back into the Bi sublattice sites; thus, excess Te vacancies and electrons are produced:[47]

$$2V'''_{Bi} + 3V^{\bullet\bullet}_{Te} + Bi'''_{Te} \rightarrow V'''_{Bi}Bi + Bi^{\times}_{Bi} + 4V^{\bullet\bullet}_{Te} + 6e' \quad (2)$$

where e′ is the excess negative carriers. The same formula is also valid for Sb'_{Te} and V'''_{Sb}. This is the *donor-like effect*. In doping and HD processing jointly optimized the p_H. In Figure 2b, we plot the zT values at 500 K as a function of p_H. Although the p_H values of

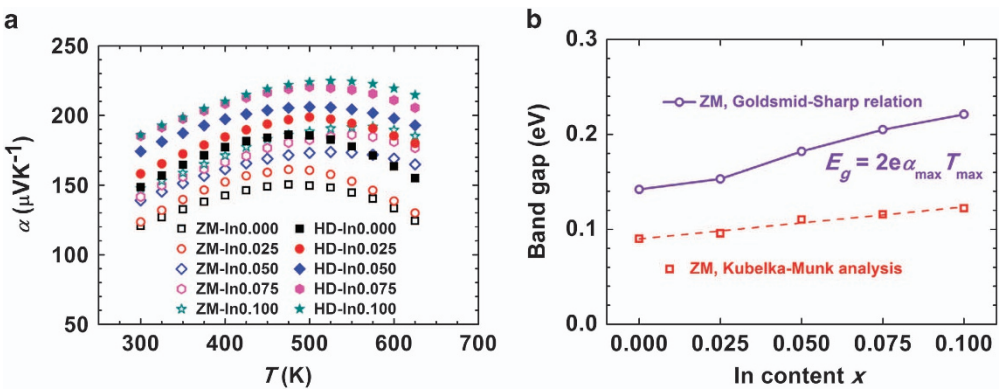

Figure 3 (**a**) Temperature dependence of Seebeck coefficient of $Bi_{0.3}Sb_{1.7-x}In_xTe_3$ zone-melted (ZM) and hot deformation (HD) samples and (**b**) band gap variation as a function of Indium (In) content in the $Bi_{0.3}Sb_{1.7-x}In_xTe_3$ ZM samples.

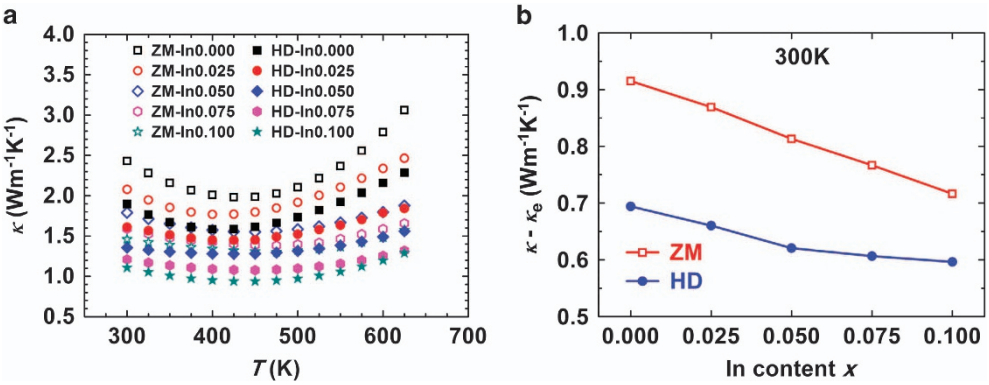

Figure 4 (**a**) Temperature dependence of total thermal conductivity κ and (**b**) room temperature lattice thermal conductivity (κ–κ_e) as a function of Indium (In) content x of all of the $Bi_{0.3}Sb_{1.7-x}In_xTe_3$ zone-melted (ZM) and hot deformation (HD) samples.

the literature and the present work are similar (in a range of 4.5×10^{19} cm^{-3} to 6×10^{19} cm^{-3}), these p_H values are obtained with a different band gap. In our In doping hot deformed samples, the band gap is broadened; as a result, the suppression of bipolar conduction facilitates higher zT values. This result is justified by the results of the band gap measurements presented in the following section.

The influence of In content x on the room temperature carrier mobility μ_H is illustrated in Figure 2c. The μ_H value decreases with increasing In content for all samples, indicating an enhanced alloy scattering of carriers.[30,45,50] In addition, the fact that the HD samples exhibit systematically lower μ_H than do their ZM counterparts implies enhanced scattering from boundaries and lattice distortions in the HD samples.[3,41] The electrical transport properties of the $Bi_{0.3}Sb_{1.7-x}In_xTe_3$ samples are plotted in Figure 2d. The increase of the In content results in a drop in the σ because of the simultaneously decreased p_H and μ_H values. Interestingly, the σ of the ZM samples exhibits a power law behavior: a crossover from $T^{-1.6}$ to $T^{-0.7}$ with increasing In content (Supplementary Figure S3). The HD samples have systematically lower σ values than their ZM counterparts because of both the reduced p_H and the reduced mobility μ_H.

Figure 3a shows the temperature-dependent Seebeck coefficient α of $Bi_{0.3}Sb_{1.7-x}In_xTe_3$ samples. The enhanced α with In doping and HD is attributed to the reduced carrier concentration and increased carrier effective mass m^* (Supplementary Figure S4). The value of m^* is estimated from the observed Seebeck coefficient and hole concentration by a single parabolic band model with acoustic phonon scattering.[30] Although the single parabolic band model is oversimplified, the trend of the m^* values is nonetheless plausible and instructive. Notably, the peak of the Seebeck coefficient shifts to higher temperatures with increasing In content because of the suppression of intrinsic excitation. As demonstrated in our previous work,[23,30,41] both the band gap and the carrier concentration are crucial for the service temperature of TE materials. For mid-temperature applications, the maximum zT must be shifted to elevated temperatures by broadening the band gap and also by increasing the concentration of *majority* carriers. However, the In doping by itself reduces the hole concentration, but widens the band gap. To determine whether this is indeed the case, we experimentally determined the band gap at different In contents by reflectance measurements. The results of the band gap derived from the reflectance data by the normalized Kubelka functions are shown in Figure 3b, and the raw reflectance data are presented in Supplementary Figure S5. Indeed, as shown in Figure 3b, the band gap increases with increasing In content, explaining the upshift of the Seebeck coefficient peak with increasing In content. Moreover, the band gap E_g of ZM $Bi_{0.3}Sb_{1.7-x}In_xTe_3$ samples was roughly estimated using the Goldsmid–Sharp relationship related to the peak α_{max} and the corresponding temperature T_{max}, that is, $E_g = 2e\alpha_{max}T_{\alpha,max}$. As displayed in Figure 3b, the value of the band gap derived by the Goldsmid–Sharp relationship is higher than the one derived optically. This discrepancy is attributed to the complex band structure and the simplifications involved in the derivation of the Goldsmid–Sharp relation. Nonetheless, the In content dependence of the band gap is qualitatively the same for both analyses.

Thermal conductivity and microstructure

The total thermal conductivity κ of all ZM and HD $Bi_{0.3}Sb_{1.7-x}In_xTe_3$ samples is plotted as a function of temperature in Figure 4a. Here, we apply a simple formula $\kappa = \kappa_e + \kappa_L + \kappa_b$, where κ_b is the bipolar contribution. The κ_e is estimated by the Wiedemann–Franz relationship $\kappa_e = L_0\sigma T$, with the Lorenz number of 2.0×10^{-8} V^{2}K^{-2} for degenerate semiconductors.[51] As shown, the reduction of κ with increasing In content is partly ascribed to the decreases in κ_e. As shown in Figure 4a, the onset of the intrinsic excitation is above 400 K. The room temperature κ_L, which is approximately equal to the (κ–κ_e) before the intrinsic excitation (where κ_b is negligible), is given as a function of In content x in Figure 4b. At elevated temperatures, the average wavelength of heat-carrying phonons decreases; as a result, the phonons are more effectively scattered by point defects. In HD samples, the microstructures may play an important role in mitigating the intrinsic conduction in addition to the increased band gap.[52,53] Indeed, the room temperature κ_L decreases with increasing In content: a 10% In doping leads to an ~20% (~ 16%) reduction in room temperature κ_L in ZM (HD) samples (Figure 4b).

Notably, the HD processing by itself can effectively reduce the κ_L, even without In doping.[3,38,40] Hence, the HD-induced microstructures, especially the atomic-scale and nanometer-scale microstructures, are worth further scrutiny. We found two noteworthy microstructural features, one at the nanoscale and one at the atomic scale. Figure 5 show two representative micrographs of HD $Bi_{0.3}Sb_{1.625}In_{0.075}Te_3$ samples to demonstrate the distorted nanoscale regions with enriched dislocations and atomic-scale lattice distortions within the five-layer (-Te$^{(1)}$-Bi-Te$^{(2)}$-Bi-Te$^{(1)}$-) sequences, respectively. The low-magnification TEM image (Figure 5a) shows several slim nanoscale distorted regions, each of which is ~10–20 nm in length and ~5 nm in width (as shown in the high-resolution TEM image, Figure 5b). The distorted regions are identified by the weak superlattice reflections around the fundamental reflections (Supplementary Figure S6); accordingly,

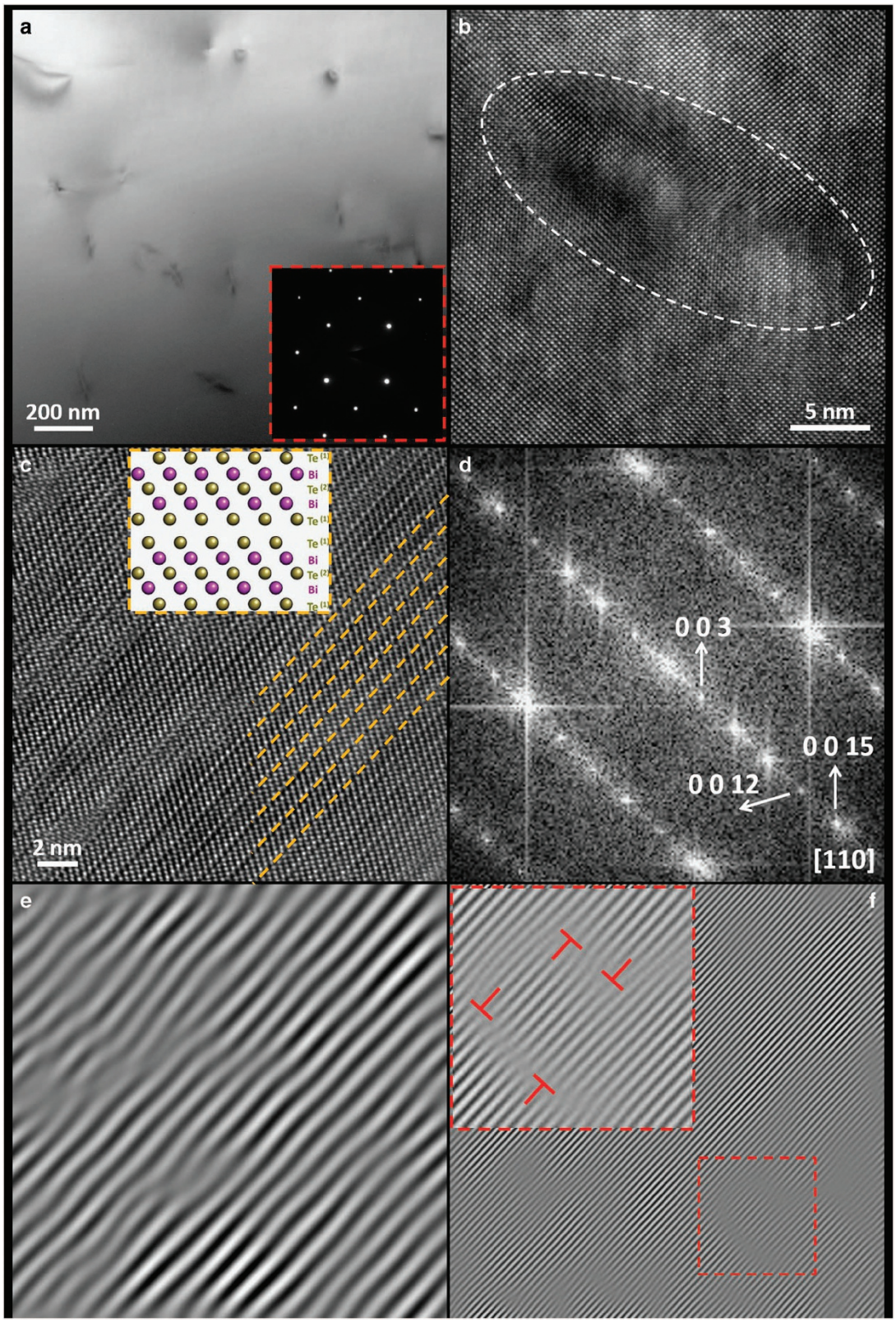

Figure 5 (**a**) Low-magnification transmission electron microscopy (TEM) image of $Bi_{0.3}Sb_{1.625}In_{0.075}Te_3$ hot deformation (HD) sample identifies crystal imperfections. The inset is a selected area electron diffraction pattern. (**b**) High-resolution transmission electron microscopy (HRTEM) image showing one nanoscale distorted region. (**c**) Lattice image showing the five-layer structure of $(Bi,Sb)_2Te_3$-based materials. The five-layer sequences are marked with yellow dashed line, and the inset is the crystal model; the fast Fourier transform (FFT) pattern of (**d**) shows 1/5 superlattice reflections, and the (003) and (0012) superlattice reflections exhibit weaker contrast than other reflections. (**e**) The inverse fast Fourier transform (IFFT) pattern obtained from (003) reflections and (**f**) the IFFT pattern obtained from (0012) reflections. The inset is an enlarged region showing dislocations.

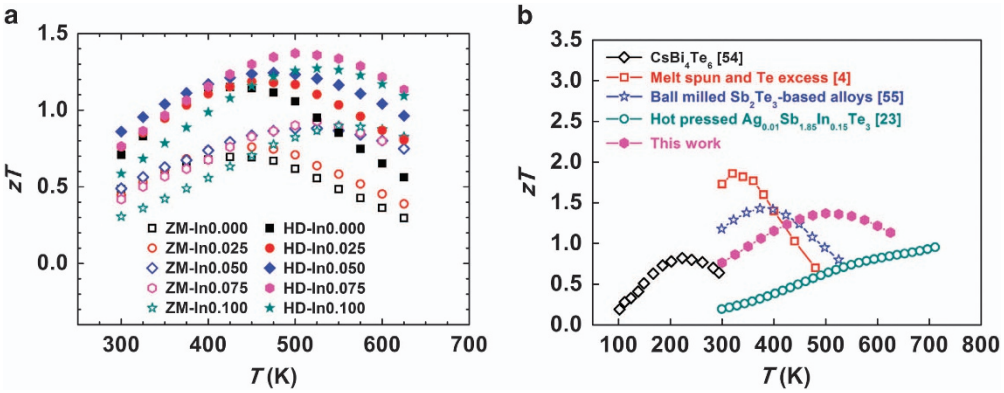

Figure 6 (**a**) Temperature dependence of zT values of all $Bi_{0.3}Sb_{1.7-x}In_xTe_3$ zone-melted (ZM) and hot deformation (HD) samples and (**b**) temperature-dependent zT values for the *p*-type V–VI compounds in different temperature ranges.[4,23,54,55]

enriched dislocations occur in the distorted region (Supplementary Figure S6), and the anomaly contrast of the distorted regions is thus due to the strain field.

The other notable microstructural feature is the high density of distortions within the five-layer sequence. The $(Bi,Sb)_2Te_3$ materials adopt a rhombohedral crystal structure (space group R-3m), and along the c-axis the structure are arranged into so-called quintuple units: $Te^{(1)}$-Bi-$Te^{(2)}$-Bi-$Te^{(1)}$. The adjacent $Te^{(1)}$ layers are bonded via a weak, van der Waals-type interaction. Strong deformation, for example, HD in the present work, would induce a high density of distortions within the five-layer sequence.[38] The five-layer structure can be clearly seen in Figure 5c. The imperfectness of these layers can be visualized via the contrast difference between (003)/(0012) and other spots in Figure 5d. After inverse Fourier transformation, the inverse fast Fourier transform pattern obtained from the (003) and (0012) reflections in Figures 5e and f clearly demonstrates a high density of distortions, for example, curved lattices or dislocations.

Furthermore, HD induces atomic-scale defects V'''_{Bi}(or V'''_{Sb}) and $V^{\bullet\bullet}_{Te}$ that further scatter the short-wavelength phonons and reduce the κ_L because of the larger mass and size differences between the occupied sites and the vacancies.[38] It is therefore plausible that the multiscale microstructures, which can range from microscale grain boundaries (Supplementary Figure S7) to the high density of nanoscale distorted regions, to lattice distortions and dislocations, and to atomic scale extrinsic and intrinsic point defects, effectively scatter heat-carrying phonons with different wavelengths and therefore reduce the lattice thermal conductivity over a wider temperature range.

zT and mechanical properties

The dimensionless figure of merit zT of all $Bi_{0.3}Sb_{1.7-x}In_xTe_3$ ZM and HD samples is shown in Figure 6a. In doping enhanced the zT at elevated temperatures (400 to 600 K) because of the increased α, decreased κ_L and suppressed bipolar effect. Meanwhile, HD processing improved zT by further optimizing the electrical properties (by the donor-like effect) and reducing the thermal conductivity. As a result, the $Bi_{0.3}Sb_{1.625}In_{0.075}Te_3$ HD sample demonstrated the highest zT value of ~1.4 at 500 K, a nearly 93% increase over that of the $Bi_{0.3}Sb_{1.7}Te_3$ ZM sample. More importantly, the averaged figure of merit zT_{av} of the $Bi_{0.3}Sb_{1.625}In_{0.075}Te_3$ HD sample is ~1.3 between 400 and 600 K, and this is to date the highest zT_{av} value of Bi_2Te_3-based alloys in this temperature regime. As shown in Figure 6b, these results fill an important gap for higher-performance TE materials between 400 and 600 K compared with other state-of-the-art TE materials.[4,23,54–59] To verify the repeatability, the $Bi_{0.3}Sb_{1.625}In_{0.075}Te_3$ HD sample was retested twice, and the results were repeatable (Supplementary Figure S8). In addition, the thermal stability of the sample was confirmed by a thermogravimetric analysis (Supplementary Figure S9).

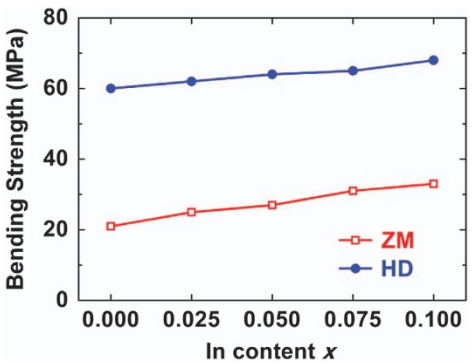

Figure 7 Bending strength as a function of Indium (In) content of the $Bi_{0.3}Sb_{1.7-x}In_xTe_3$ bulk samples before and after hot deformation (HD).

Notwithstanding that zT is the material parameter of utmost importance in TE study, the mechanical properties are crucial from an application standpoint. In particular, the material should not only have high zT values over a wide temperature range but should also be easily cut and of high bending strength. We found that our $Bi_{0.3}Sb_{1.7-x}In_xTe_3$ ZM and HD samples had improved mechanical properties (Figure 7).

In summary, we have successfully shifted the service temperature of *p*-type $(Bi,Sb)_2Te_3$ from near room temperature to the mid-temperature range via the synergies of point defect engineering, multiscale phonon scattering and band engineering. In doping broadened the band gap and thus suppressed the detrimental bipolar effect that would otherwise be present in the mid-temperature range. In dopants, in addition to providing the donor-like effect, optimized the carrier concentration. Furthermore, the In doping induced extrinsic and intrinsic point defects that, along with the multiscale microstructures created by HD, helped suppress the lattice thermal conductivity. The integration of all of these effects in the $Bi_{0.3}Sb_{1.625}In_{0.075}Te_3$ HD sample led to a zT of ~1.4 at 500 K and a state-of-the-art zT_{av} of ~1.3 between 400 and 600 K, along with improved mechanical properties. These results demonstrated the efficacy of the doping/hot deformation procedure and the promise of *p*-type hot deformed $Bi_{0.3}Sb_{1.7-x}In_xTe_3$ materials for use in mid-temperature power generation.

CONFLICT OF INTEREST

The authors declare no conflict of interest.

ACKNOWLEDGEMENTS

The work was supported by the National Basic Research Program of China (2013CB632503), the Nature Science Foundation of China (51271165 and 51171171) and the Program for New Century Excellent Talents in University (NCET-12-0495). Jiaqing He acknowledges the support from the Shenzhen Science and Technology Plan Project (No. ZDSYS20141118160434515). Jian He acknowledges the support of the NSF-DMR 1307740.

1 DiSalvo, F. J. Thermoelectric cooling and power generation. *Science* **285**, 703–706 (1999).
2 Tritt, T. M. Thermoelectric materials - holey and unholey semiconductors. *Science* **283**, 804–805 (1999).
3 Zhu, T. J., Xu, Z., He, J., Shen, J., Zhu, S., Hu, L., Tritt, T.M., & Zhao, X. A hot deformation induced bulk nanostructuring of unidirectionally grown p-type $(Bi,Sb)_2Te_3$ thermoelectric materials. *J. Mater. Chem.* **1**, 11589–11594 (2013).
4 Il Kim, S. I., Lee, K. H., Mun, H. A., Kim, H. S., Hwan, S. W., Ro, J W., Yan, D, J., Shi, W. H., Li, X. S., Lee, Y. H., Snyder, G. J. & Kim, S. W. Dense dislocation arrays embedded in grain boundaries for high-performance bulk thermoelectrics. *Science* **348**, 109–114 (2015).
5 Biswas, K., He, J., Blum, I. D., Wu, C.-I., Hogan, T. P., Seidman, D. N., Dravid, V. P. & Kanatzidis, M. G. High-performance bulk thermoelectrics with all-scale hierarchical architectures. *Nature* **489**, 414–418 (2012).
6 Heremans, J. P., Jovovic, V., Toberer, E. S., Saramat, A., Kurosaki, K., Charoenphakdee, A., Yamanaka, S. & Snyder, G. J. Enhancement of thermoelectric efficiency in PbTe by distortion of the electronic density of states. *Science* **321**, 554–557 (2008).
7 Liu, W., Tan, X., Yin, K., Liu, H., Tang, X., Shi, J., Zhang, Q. & Uher, C. Convergence of conduction bands as a means of enhancing thermoelectric performance of n-type $Mg_2Si_{1-x}Sn_x$ solid solutions. *Phys Rev. Lett.* **108**, 166601 (2012).
8 Liu, X., Zhu, T., Wang, H., Hu, L., Xie, H., Jiang, G., Snyder, G. J. & Zhao, X. Low electron scattering potentials in high performance $Mg_2Si_{0.45}Sn_{0.55}$ based thermoelectric solid solutions with band convergence. *Adv. Energy Mater.* **3**, 1238–1244 (2013).
9 Pei, Y., Shi, X., LaLonde, A., Wang, H., Chen, L. & Snyder, G. J. Convergence of electronic bands for high performance bulk thermoelectrics. *Nature* **473**, 66–69 (2011).
10 Shi, X., Yang, J., Salvador, J. R., Chi, M., Cho, J. Y., Wang, H., Bai, S., Yang, J., Zhang, W. & Chen, L. Multiple-filled skutterudites: high thermoelectric figure of merit through separately optimizing electrical and thermal transports. *J. Am. Chem. Soc.* **133**, 7837–7846 (2011).
11 Xie, H., Wang, H., Pei, Y., Fu, C., Liu, X., Snyder, G. J., Zhao, X. & Zhu, T. Beneficial contribution of alloy disorder to electron and phonon transport in half-Heusler thermoelectric materials. *Adv. Funct. Mater.* **23**, 5123–5130 (2013).
12 Fu, C., Bai, S., Liu, Y., Tang, Y., Chen, L., Zhao, X. & Zhu, T. Realizing high figure of merit in heavy-band p-type half-Heusler thermoelectric materials. *Nat. Commun.* **6**, 8144 (2015).
13 Jiang, G., He, J., Zhu, T., Fu, C., Liu, X., Hu, L. & Zhao, X. High performance $Mg_2(Si,Sn)$ solid solutions: a point defect chemistry approach to enhancing thermoelectric properties. *Adv. Funct. Mater.* **24**, 3776–3781 (2014).
14 Zhu, T. J., Fu, C. G., Xie, H. H., Liu, Y. T. & Zhao, X. B. High efficiency half-Heusler thermoelectric materials for energy harvesting. *Adv. Energy Mater.* **5**, 1500588 (2015).
15 Barr, T. D. & Dahlen, F. A. Brittle frictional mountain building 2 thermal structure and heat-budget. *J. Geophys. Res.* **94**, 3923–3947 (1989).
16 Hsu, C. T., Huang, G. Y., Chu, H. S., Yu, B. & Yao, D. J. Experiments and simulations on low-temperature waste heat harvesting system by thermoelectric power generators. *Appl. Energy* **88**, 1291–1297 (2011).
17 Wu, C. Analysis of waste-heat thermoelectric power generators. *Appl. Therm. Eng.* **16**, 63–69 (1996).
18 Ono, K. & Suzuki, R. O. Thermoelectric power generation: converting low grade heat into electricity. *J. Miner. Met. Mater. Soc.* **50**, 49–51 (1998).
19 Sumithra, S., Takas, N. J., Misra, D. K., Nolting, W. M., Poudeu, P. F. P. & Stokes, K. L. Enhancement in thermoelectric figure of merit in nanostructured Bi_2Te_3 with semimetal nanoinclusions. *Adv. Energy Mater.* **1**, 1141–1147 (2011).
20 Yang, J. H. & Caillat, T. Thermoelectric materials for space and automotive power generation. *MRS Bull.* **31**, 224–229 (2006).
21 Wang, S, Tan, G., Xie, W., Zheng, G., Li, H., Yang, J. & Tang, X. Enhanced thermoelectric properties of $Bi_2(Te_{1-x}Se_x)_3$-based compounds as n-type legs for low-temperature power generation. *J. Mater. Chem.* **22**, 20943–20951 (2012).
22 Liu, W., Lukas, K. C., McEnaney, K., Lee, S., Zhang, Q., Opeil, C. P., Chen, G. & Ren, Z. Studies on the Bi_2Te_3-Bi_2Se_3-Bi_2S_3 system for mid-temperature thermoelectric energy conversion. *Energy Environ. Sci.* **6**, 552–560 (2013).
23 Hua, L. P., Zhu, T. J., Yue, X. Q., Liu, X. H., Wang, Y. G., Xu, Z. J. & Zhao, X. B. Enhanced figure of merit in antimony telluride thermoelectric materials by In-Ag co-alloying for mid-temperature power generation. *Acta Mater.* **85**, 270–278 (2015).
24 Kohler, H. Non-parabplic E(K) relation of lowest conduction-band in Bi_2Te_3. *Phys. Status Solidi B Basic Res.* **73**, 95–104 (1976).
25 Black, J., Conwell, E. M., Seigle, L. & Spencer, C. W. Electrical and optical properties of some M_2V-BN_3VI-B semiconductors. *J. Phys. Chem. Solids* **2**, 240–251 (1957).
26 Pei, Y. Z., Wang, H. & Snyder, G. J. Band engineering of thermoelectric materials. *Adv. Mater.* **24**, 6125–6135 (2012).
27 Langhammer, H. T., Stordeur, M., Sobotta, H. & Riede, V. Ir transmission investigations of Sb_2Te_3 single-crystals. *Phys. Status Solidi B Basic Res.* **123**, K47–K51 (1984).
28 Sehr, R. & Testardi, L. R. Optical properties of p-type Bi_2Te_3-Sb_2Te_3 alloys between 2-15 microns. *J. Phys. Chem. Solids.* **23**, 1219–1224 (1962).
29 Stary, Z., Horak, J., Stordeur, M. & Stolzer, M. Antisite defects in $Sb_{2-x}Bi_xTe_3$ mixed crystals. *J. Phys. Chem. Solids* **49**, 29–34 (1988).
30 Hu, L.-P., Zhu, T.-J., Wang, Y.-G., Xie, H.-H., Xu, Z.-J. & Zhao, X.-B. Shifting up the optimum figure of merit of p-type bismuth telluride-based thermoelectric materials for power generation by suppressing intrinsic conduction. *NPG Asia Mater.* **6**, e88 (2014).
31 Drasar, C., Hovorková, A., Losták, P., Kong, H., Li, C.-P. & Uher, C. Figure of merit of quaternary $(Sb_{0.75}Bi_{0.25})_{2-x}In_xTe_3$ single crystals. *J. Appl. Phys.* **104**, 023701 (2008).
32 Hu, L. P., Zhu, T. J., Liu, X. H. & Zhao, X. B. Point defect engineering of high-performance bismuth-telluride-based thermoelectric materials. *Adv. Funct. Mater.* **24**, 5211–5218 (2014).
33 Pan, Y., Wei, T. R., Cao, Q. & Li, J. F. Mechanically enhanced p- and n-type Bi_2Te_3-based thermoelectric materials reprocessed from commercial ingots by ball milling and spark plasma sintering. *Mater. Sci. Eng. B Adv. Funct. Solid State Mater.* **197**, 75–81 (2015).
34 Pan, Y., Wei, T. R., Wu, C. F. & Li, J. F. Electrical and thermal transport properties of spark plasma sintered n-type $Bi_2Te_{3-x}Se_x$ alloys: the combined effect of point defect and Se content. *J. Mater. Chem. C* **3**, 10583–10589 (2015).
35 Wang, H., Gibbs, Z. M., Takagiwa, Y. & Snyder, G. J. Tuning bands of PbSe for better thermoelectric efficiency. *Energy Environ. Sci.* **7**, 804–811 (2014).
36 Fu, C. G., Zhu, T. J., Liu, Y. T., Xie, H. H. & Zhao, X. B. Band engineering of high performance p-type FeNbSb based half-Heusler thermoelectric materials for figure of merit $zT > 1$. *Energy Environ. Sci.* **8**, 216–220 (2015).
37 Hu, L., Gao, H., Liu, X., Xie, H., Shen, J., Zhu, T. & Zhao, X. Enhancement in thermoelectric performance of bismuth telluride based alloys by multi-scale microstructural effects. *J. Mater. Chem.* **22**, 16484–16490 (2012).
38 Hu, L., Wu, H., Zhu, T., Fu, C., He, J., Ying, P. & Zhao, X. Tuning multiscale microstructures to enhance thermoelectric performance of n-type bismuth-telluride-based solid solutions. *Adv. Energy Mater.* **5**, 1500411 (2015).
39 Wu, H. J., Zhao, L.-D., Zheng, F. S., Wu, D., Pei, Y. L., Tong, X., Kanatzidis, M. G. & He, J. Q. Broad temperature plateau for thermoelectric figure of merit $ZT > 2$ in phase-separated $PbTe_{0.7}S_{0.3}$. *Nat. Commun.* **5**, 4515 (2014).
40 Shen, J.-J., Zhu, T.-J., Zhao, X.-B.Z, Zhang, S.-N., Yang, S.-H. & Yin, Z.-Z. Recrystallization induced in situ nanostructures in bulk bismuth antimony tellurides: a simple top down route and improved thermoelectric properties. *Energy Environ. Sci.* **3**, 1519–1523 (2010).
41 Xu, Z. J., Hu, L. P., Ying, P. J., Zhao, X. B. & Zhu, T. J. Enhanced thermoelectric and mechanical properties of zone melted p-type $(Bi,Sb)_2Te_3$ thermoelectric materials by hot deformation. *Acta Mater.* **84**, 385–392 (2015).
42 Gibbs, Z. M., LaLonde, A. & Snyder, G. J. Optical band gap and the Burstein-Moss effect in iodine doped PbTe using diffuse reflectance infrared Fourier transform spectroscopy. *New J. Phys.* **15**, 075020 (2013).
43 Horak, J., Cermak, K. & Koudelka, L. Energy formation of antisite defects in doped Sb_2Te_3 and Bi_2Te_3 crystals. *J. Phys. Chem. Solids* **47**, 805–809 (1986).
44 Termentzidis, K., Pokropyvnyy, O., Woda, M., Xiong, S., Chumakov, Y., Cortona, P. & Volz, S. Large thermal conductivity decrease in point defective Bi_2Te_3 bulk materials and superlattices. *J. Appl. Phys.* **113**, 013506 (2013).
45 Horak, J., Lostak, P. & Benes, L. Suppression of antistructural defects in crystals by an increased polarization of bonds. *Philos. Mag. B Phys. Condens. Matter Stat. Mech. Electron. Opt. Magn. Prop.* **50**, 665–671 (1984).
46 Lostak, P., Novotny, R., Kroutil, J. & Stary, Z. Optical-properties of $Sb_{2-x}In_xTe_3$ single-crystals. *Phys. Status Solidi A Appl. Res.* **104**, 841–848 (1987).
47 Navratil, J., Stary, Z. & Plechacek, T. Thermoelectric properties of p-type antimony bismuth telluride alloys prepared by cold pressing. *Mater. Res. Bull.* **31**, 1559–1566 (1996).
48 Schultz, J. M., Tiller, W. A. & McHugh, J. P. Effects of heavy deformation and annealing on electrical properties of Bi_2Te_3. *J. Appl. Phys.* **33**, 2443–2450 (1962).
49 Ionescu, R., Jaklovszky, J., Nistor, N. & Chiculita, A. Grain-size effects on thermo-electrical properties of sintered solid-solutions based on Bi_2Te_3. *Phys. Status Solidi A Appl. Res.* **27**, 27–34 (1975).
50 Birkholz, U. Untersuchung der intermetallischen verbindung Bi_2Te_3 sowie der festen losungen $Bi_{2-x}Sb_xTe_3$ und $Bi_2Te_{3-x}Se_x$ hinsichtlich ihrer eignung als material fur halbleiter-thermoelemente. *Z. Phys. Chem.* **13**, 780–792 (1958).
51 Mi, J. L., Zhao, X. B., Zhu, T. J. & Tu, J. P. Improved thermoelectric figure of merit in n-type $CoSb_3$ based nanocomposites. *Appl. Phys. Lett.* **92**, 029905 (2008).
52 Wang, S., Yang, J., Toll, T., Yang, J., Zhang, W. & Tang, X. Conductivity-limiting bipolar thermal conductivity in semiconductors. *Sci Rep.* **5**, 10136 (2015).
53 Bahk, J. H. & Shakouri, A. Enhancing the thermoelectric figure of merit through the reduction of bipolar thermal conductivity with heterostructure barriers. *Appl. Phys. Lett.* **105**, 052106 (2014).

54 Chung, D. Y., Hogan, T., Brazis, P., Kannewurf, C., Bastea, M., Uher, C. & Kanatzidis, M. G. CsBi4Te6: a high-performance thermoelectric material for low-temperature applications. *Science.* **287**, 1024–1027 (2000).
55 Poudel, B., Hao, Q., Ma, Y., Lan, Y., Minnich, A., Yu, B., Yan, X., Wang, D., Muto, A., Vashaee, D., Chen, X., Liu, J., Dresselhaus, M. S., Chen, G. & Ren, Z. High-thermoelectric performance of nanostructured bismuth antimony telluride bulk alloys. *Science.* **320**, 634–638 (2008).
56 Li, Y., Li, D., Qin, X., Yang, X., Liu, Y., Zhang, J., Dou, Y., Song, C. & Xin, H. Enhanced thermoelectric performance through carrier scattering at heterojunction potentials in BiSbTe based composites with Cu_3SbSe_4 nanoinclusions. *J. Mater. Chem. C* **3**, 7045–7052 (2015).
57 Li, J., Tan, Q., Li, J.-F., Liu, D.-W., Li, F., Li, Z.-Y., Zou, M. & Wang, K. BiSbTe-based nanocomposites with high ZT : the effect of SiC nanodispersion on thermoelectric properties. *Adv. Funct. Mater.* **23**, 4317–4323 (2013).
58 Xie, W., He, J., Kang, H. J., Tang, X., Zhu, S., Laver, M., Wang, S., Copley, J. R. D., Brown, C. M., Zhang, Q. & Tritt, T. M. Identifying the specific nanostructures responsible for the high thermoelectric performance of $(Bi,Sb)_2Te_3$ nanocomposites. *Nano Lett.* **10**, 3283–3289 (2010).
59 Xie, W. J., Tang, X. F., Yan, Y. G., Zhang, Q. J. & Tritt, T. M. Unique nanostructures and enhanced thermoelectric performance of melt-spun BiSbTe alloys. *Appl. Phys. Lett.* **94**, 102111 (2009).

Supplementary Information accompanies the paper on the NPG Asia Materials website (http://www.nature.com/am)